



Title	On the implementation of faults in finite-element glacial isostatic adjustment models
Author(s)	Steffen, R; Wu, P; Steffen, H; Eaton, DW
Citation	Computers and Geosciences, 2014, v. 62, p. 150-159
Issued Date	2014
URL	http://hdl.handle.net/10722/192182
Rights	NOTICE: this is the author's version of a work that was accepted for publication in Computers & Geosciences. Changes resulting from the publishing process, such as peer review, editing, corrections, structural formatting, and other quality control mechanisms may not be reflected in this document. Changes may have been made to this work since it was submitted for publication. A definitive version was subsequently published in Computers & Geosciences, 2014, v. 62, p. 150-159. DOI: 10.1016/j.cageo.2013.06.012

On the implementation of faults in finite-element glacial isostatic adjustment models

Rebekka Steffen ^{a,*}, Patrick Wu ^a, Holger Steffen ^{a,b},

David W. Eaton ^a

^a*Department of Geoscience, University of Calgary, 2500 University Drive NW, Calgary,
Alberta, T2N 1N4, Canada*

^b*now at: Lantmäteriet, Lantmäterigatan 2c, 80182 Gävle, Sweden*

Abstract

Stresses induced in the crust and mantle by continental-scale ice sheets during glaciation [has](#) triggered earthquakes along pre-existing faults, commencing near the end of the deglaciation. In order to get a better understanding of the relationship between glacial loading/unloading and fault movement due to the spatio-temporal evolution of stresses, a commonly used model for glacial isostatic adjustment (GIA) is extended by including a fault structure. Solving this problem is enabled by development of a workflow involving three cascaded finite-element simulations. Each step has identical lithospheric and mantle structure and properties, but evolving stress conditions along the fault.

The purpose of the first simulation is to compute the spatio-temporal evolution of rebound stress when the fault is tied together. An ice load with a parabolic profile and simple ice history is applied to represent glacial loading of the Laurentide Ice Sheet. The results of the first step describes the evolution of the stress and displacement induced by the rebound process. The second step in the procedure augments the results of the first, by computing the spatio-temporal evolution of total stress (i. e. rebound stress plus tectonic background

stress and overburden pressure) and displacement with reaction forces that can hold the model in equilibrium. The background stress is estimated by assuming that the fault is in frictional equilibrium before glaciation. The third steps simulates fault movement induced by the spatio-temporal evolution of total stress by evaluating fault stability in a subroutine. If the fault remains stable, no movement occurs; in case of fault instability, the fault displacement is computed.

We show an example of fault motion along a 45°-dipping fault at the ice-sheet centre for a two-dimensional model. Stable conditions along the fault are found during glaciation and the initial part of deglaciation. Before deglaciation ends, the fault starts to move, and fault offsets of up to 22 m are obtained. A fault scarp at the surface of 19.74 m is determined. The fault is stable in the following time steps with a high stress accumulation at the fault tip. Along the upper part of the fault, GIA stresses are released in one earthquake.

Key words: Glacial isostatic adjustment; Fault; Finite element modelling; Flexural stresses; ABAQUS

* Corresponding author.

Email address: rsteffen@ucalgary.ca (Rebekka Steffen).

1 Introduction

2 In the Earth's crust, stress can be subdivided into tectonic background stress, over-
3 burden pressure, and pore-fluid pressure. The superposition of the first two and the
4 variation of the third part are factors in controlling movement along faults [e. g.
5 Twiss & Moores, 2007]. Furthermore, stresses due to sedimentation and erosion
6 contribute to the total stress field. In deglaciated regions, an additional stress must
7 be considered: the rebound stress, which is related to rebounding of the crust and
8 mantle after deglaciation [e. g. Wu & Hasegawa, 1996a, Wu, 1996].

9 During the growth of a continental ice sheet, the lithosphere under the ice load is
10 deformed into the mantle and the removal of the ice load during deglaciation initi-
11 ates a rebound process. The uplift is well known in formerly glaciated areas, e. g.
12 North America and Scandinavia, and in currently deglaciating areas, e. g. Alaska,
13 Antarctica, and Greenland. The whole process of subsiding and uplifting during the
14 growth and melting of an ice load and all related phenomena is known as glacial
15 isostatic adjustment (GIA).

16 During the process of glaciation, the surface of the lithosphere is depressed un-
17 derneath the ice load and compressional flexural stresses are induced in the upper
18 lithosphere, whereas the bottom of the lithosphere experiences tensional flexural
19 stresses [e. g. Adams, 1989a, Wu & Hasegawa, 1996a]. An additional vertical stress
20 due to the ice load is present, which decreases to zero during deglaciation [e. g. Wu
21 & Hasegawa, 1996a]. During rebound, flexural stresses relax slowly. These stresses
22 are able to change the original stress directions and regime [Wu, 1996].

23 In a thrusting background stress regime with the maximum principal stress in the
24 horizontal direction and the minimum principal stress in the vertical direction, the
25 stresses of flexure and vertical loading lead to stable conditions along a fault dur-

26 ing loading [Johnston, 1987], and unstable conditions during deglaciation and af-
27 terwards [Wu & Hasegawa, 1996a,b]. This stress regime is dominant in formerly
28 glaciated continental areas; however, in some areas normal or strike-slip regimes
29 occur [e. g. Adams, 1989b, Wu, 1996, 1997, Heidbach et al., 2008, Lund et al.,
30 2009, Mazzotti & Townend, 2010, Steffen & Wu, 2011, Steffen et al., 2012].

31 In the presence of ice, the vertical load increases the minimum principal stress, but
32 horizontal stress (maximum principal stress) is also increased due to flexure. After
33 glacial maximum, the mass of the ice load decreases and the vertical stress induced
34 by this load decreases to zero at the end of the deglaciation. But at this time point,
35 the flexural stress in the horizontal direction still exceeds the initial state, leaving an
36 additional stress in the crust that is able to reactivate a pre-existing fault structure
37 [Wu & Hasegawa, 1996a].

38 Several faults with high fault scarps, which document the occurrence of large earth-
39 quakes during and after the end of deglaciation, have been identified in North Amer-
40 ica and Europe [e. g. Kujansuu, 1964, Lagerbäck, 1978, Olesen, 1988, Dyke et al.,
41 1991]. Field investigations indicate that post-glacial unloading and rebound led to
42 the formation or re-activation of faults in continental shields [e. g. Lagerbäck, 1978,
43 Adams, 1989a]. Furthermore, a formerly glaciated area is generally characterized
44 by moderate seismic activity today.

45 During the last 15 years, various numerical models have been developed to simu-
46 late the occurrence of earthquakes during the glacial period. Of these, two different
47 types of models exist to investigate fault stability. The first type has been employed
48 by Wu [1996, 1997], Wu & Hasegawa [1996a,b], Johnston et al. [1998], Klemann
49 & Wolf [1998], Lund [2005] and Lund et al. [2009] using either the finite-element
50 methodology (FEM) or spectral method. These models are based on general GIA
51 models including crust and mantle; they have no explicit fault structure, but con-

52 sidered instead virtual faults, which have no effect on the surrounding stress or
53 displacement. This approach is normally used to analyse the isostatic adjustment
54 process in a viscoelastic Earth, in which the lateral boundaries do not have any
55 plate velocity applied. Stress changes and stability of pre-existing faults are eval-
56 uated at assumed fault locations [Wu & Hasegawa, 1996a]. Since, fault surfaces
57 are not included in these models, the estimation of the total stress is made after the
58 modelling of GIA (see Section 2). Therefore, it is not possible to obtain fault slip
59 values with these types of models without modifications.

60 The rebound stress obtained from these models is combined with the horizontal and
61 vertical background stresses, which are taken into account in the computation of
62 fault stability. Assuming a thrusting tectonic background stress regime, the area be-
63 low an ice sheet tends to be stable during glaciation and deglaciation, but becomes
64 unstable immediately after the end of deglaciation [Wu & Hasegawa, 1996a]. Con-
65 versely, faults in a normal or strike-slip regime are stable after deglaciation, but
66 may be unstable during glaciation [Wu & Hasegawa, 1996a]. A comparison of the
67 present day stress orientation in northeastern Canada inferred from focal mecha-
68 nism data with predictions from this class of GIA models exhibits large differences
69 indicating that these GIA models do not adequately capture stress changes due to
70 local fault zones [see Steffen et al., 2012].

71 The second type of GIA induced faulting models was developed by Hetzel & Ham-
72 pel [2005], Hampel & Hetzel [2006] and Hampel et al. [2009]. These models in-
73 clude a real fault, but only consist of a lithospheric layer that has horizontal plate
74 velocities prescribed at the lateral boundaries. However, the ~~process of~~ glaciation
75 and deglaciation depends not only on the lithosphere but also on the underlying
76 mantle. Therefore, the inclusion of a deeper mantle in the models is necessary to
77 obtain correct displacement and stress values for the GIA process. Thus, although a

78 fault is already included in these models, fault movement is partially driven by the
79 horizontal plate velocities and rebound stress is not completely taken into account.
80 The results by Hampel et al. [2009] show stable conditions along the fault during
81 glaciation for a thrusting regime. During and after the end of deglaciation the fault
82 starts to move.

83 In general, both type of models yield similar results. However, the former models
84 do not include an explicit fault, while the latter models do not include the influence
85 of the deeper mantle or rebound stress. Therefore, both models provide only an ap-
86 proximate representation of fault movement in formerly glaciated areas.

87 In this study, we will present a new two-dimensional (2D) model based on the
88 ABAQUS FEM [Hibbitt et al., 2011], which combines the aforementioned model
89 types by using a defined fault in a general GIA model. The purpose of this paper is
90 to present a new approach, which allows the estimation of fault slip and activation
91 time under realistic rebound conditions. As this is a preliminary investigation, it
92 is not our goal to match modelled results to observed data; consequently detailed
93 earth and ice models are not considered. Rather, our aim is to extend and adapt
94 existing GIA models for fault slip estimation.

95 The theoretical background of fault stability and the application of FEM for GIA
96 purposes is discussed in the following two sections. In the fourth section, the model
97 setup is summarized. This is followed by results for a simple example that includes
98 a fault.

99 **2 Stress analysis**

100 In order to evaluate the stability of a fault in a GIA model we need to model the
101 spatio-temporal evolution of the stress. The state of stress in a region is described

102 by the magnitude of vertical and horizontal stresses, and in an area affected by GIA,
 103 this consists of the overburden pressure, tectonic background stress, and a rebound
 104 component to be determined by the model.

105 2.1 Fault stability

106 In a stable crust, where no faults exist, rebound stresses are not large enough to
 107 fracture rocks and generate earthquakes [e. g. Quinlan, 1984]. However, the crust
 108 is not always in a stable state, because it is interspersed with fractures and faults
 109 that constitute zones of weaknesses [e. g. Twiss & Moores, 2007]. The stress con-
 110 ditions in weak but stable, zones in a rock mass can be represented by using a Mohr
 111 diagram (Fig. 1).

112 Figure 1

113 The line of failure (black and red lines in Fig. 1) gives information about the sta-
 114 bility and frictional behaviour of a fault or rock mass, and relates the shear stress
 115 τ to the normal stress σ_n . The difference in shear stress between line of failure and
 116 Mohr circle is used to estimate the stability of the crust or a fault, which is known
 117 as the Coulomb Failure Stress (*CFS*) [Harris, 1998]. The *CFS* at a specific normal
 118 stress σ_n is defined as:

$$\begin{aligned}
 CFS &= \tau - \tau', \\
 &= \tau - (\mu (\sigma_n - P_f) + C), \\
 &= \frac{\sigma_1 - \sigma_3}{2} |\sin 2\Theta| - \mu \left(\frac{\sigma_1 + \sigma_3}{2} + \frac{\sigma_1 - \sigma_3}{2} \cos 2\Theta \right) + \mu P_f - C, \\
 &= \frac{\sigma_1 - \sigma_3}{2} (|\sin 2\Theta| - \mu \cos 2\Theta) - \mu \frac{\sigma_1 + \sigma_3}{2} + \mu P_f - C. \quad (1)
 \end{aligned}$$

119 In equation (1), negative *CFS* values indicate stable conditions and a change to pos-

120 itive values refers to a change from stability to instability along the fault, creating
121 a state where earthquakes may occur.

122 The *CFS* depends on the maximum (σ_1) and minimum (σ_3) principal stresses, an
123 angle Θ , which is related to the angle of the fault α , coefficient of friction μ , cohe-
124 sion C , and pore-fluid pressure P_f (see below).

125 The angle Θ in equation (1) is related to α [Twiss & Moores, 2007]:

$$2\Theta = 180^\circ - 2\alpha - \arctan\left(\frac{2S_{13}}{S_{11} + S_{33}}\right), \quad (2)$$

126 with S_{ij} ($\{i, j\} = \{1, 3\}$) as the components of the stress tensor. The last term
127 in this equation depends on the stress regime and describes the change of σ_1 with
128 respect to the horizontal or vertical direction. In an undisturbed thrust/reverse or
129 normal stress state, with σ_1 and σ_3 being horizontal and/or vertical, the shear stress
130 component S_{13} is zero, and equation (2) becomes $2\Theta = 180^\circ - 2\alpha$.

131 2.2 Overburden pressure

132 The overburden pressure is the weight of the overlying rocks. It depends upon on
133 the gravity g_{layer} and density ρ_{layer} of the rocks lying above a depth z . Furthermore,
134 the effect of fluid-filled pore spaces (P_f) in the rock contributes to the overburden
135 pressure. The overburden pressure is described by [Twiss & Moores, 2007]:

$$S_V = \int \rho_{layer} g_{layer} dz - P_f = \int (1 - \lambda_f) \rho_{layer} g_{layer} dz, \quad (3)$$

136 with λ_f as the ratio of fluid to rock density and is the same for all tectonic back-
137 ground regimes. This equation involves the assumption that the pore pressure is a
138 linear function of the overburden pressure.

139 2.3 Tectonic background stress

140 The tectonic background stress includes both the maximum horizontal background
141 stress (S_H) and the minimum horizontal background stress (S_h). The latter can be
142 similar in magnitude to the former, but might differ by several MPa depending on
143 the tectonic environment.

144 In several studies, the maximum horizontal background stress is calculated assum-
145 ing that the fault was at frictional equilibrium before the onset of glacial cycles.
146 Although, not all faults are optimally orientated [Abers, 2009]; the stress condi-
147 tions generally assumed are for optimally orientated faults. For example, glacially
148 induced faults (GIFs) generally have high angles of 50° to 80° [Fenton, 1994, Juh-
149 lin et al., 2009, Brandes et al., 2012]. They are often assumed to have been active
150 as normal faults before being reactivated as thrust faults [e. g. Adams, 1989a]. As
151 steep dipping faults are not optimally orientated in a thrusting regime, the assump-
152 tion of optimally orientated faults in such regions is not generally applicable and
153 the horizontal background stress may depend on the fault angle. Thus, an equation
154 for a generally oriented (including non-optimally oriented) fault at frictional equi-
155 librium is needed.

156 To obtain an equation for every fault angle, several assumptions have to be made. A
157 rock mass with no fractures has a higher cohesion than pre-existing faults [Lanaro
158 et al., 2006]. Furthermore, if no optimally orientated fault exists in this rock mass
159 or has a higher cohesion, other faults with different angles might be reactivated
160 [e. g. Abers, 2009]. To estimate the necessary amount of tectonic background stress
161 to allow slip along non-optimally orientated faults, the fault is assumed to be in
162 frictional equilibrium for all depths in the absence of any ice loads.

163 The *CFS* is used to estimate the maximum horizontal component S_H of the stress

164 in a thrusting regime:

$$S_H = \frac{S_V [\mu - \mu \cos 2\Theta + |\sin 2\Theta|] + 2CFS^{BG} - 2\mu P_f + 2C}{- [\mu \cos 2\Theta + \mu - |\sin 2\Theta|]}, \quad (4)$$

165 where CFS^{BG} denotes the stability of the fault or rock mass before glaciation.

166 For an optimally orientated fault angle, equation (4) reduces to the same equation
167 as used commonly (e. g. Zoback & Townend [2001]). Furthermore, equation (4) is
168 only valid along the fault plane. As no other constraints are given for the tectonic
169 background stress in the crust in absence of faults, equation (4) is assumed to be
170 applicable to other parts of the critically stressed crust [Zoback & Townend, 2001].
171 The assumption of large magnitudes for the tectonic background stress is one
172 scenario allowing non-optimally orientated faults to break. Other time-dependant
173 changes in the pore-fluid pressure or cohesion are possible. However, neither of the
174 latter scenarios can be realized in our FE model, as cohesion cannot be defined for
175 a fault surface in ABAQUS, and the change in pore-fluid pressure with time due to
176 glaciation and deglaciation is insufficiently studied.

177 2.4 GIA stress obtained from ABAQUS

178 Several methods have been developed to model the process of GIA [see Steffen &
179 Wu, 2011, for a review]. Each method has its own advantages and disadvantages,
180 but in general, all methods give reasonably similar results [Spada et al., 2011].
181 The FEM has become more popular because it can take into account non-linear
182 rheology [Wu, 1999, van der Wal et al., 2010] and lateral heterogeneities such as
183 lateral viscosity [Wang & Wu, 2006, Wu et al., 2013] and density variations [Ni &
184 Wu, 1998, Schmidt et al., 2012]. Our methodology is based on the approach by Wu
185 [2004].

186 In commercial FE packages [e. g. ABAQUS; Hibbitt et al., 2011] the equation of
 187 motion,

$$\nabla \cdot \mathbf{S} = 0, \quad (5)$$

188 is solved with \mathbf{S} as the stress tensor. However, this equation is not applicable to
 189 geophysical problems involving elastic deformation of long wavelengths [Cathles,
 190 1975, Wu, 1992, 2004]. If inertial force, self-gravitation, and internal buoyancies
 191 are neglected, the momentum equation in geophysical applications for a flat Earth
 192 is of the form [Wu, 2004]:

$$\nabla \cdot \mathbf{S}^{GIA} - \rho_0 g_0 \nabla u_z = 0, \quad (6)$$

193 where ρ_0 and g_0 represent the density and gravity for the initial background state,
 194 and u_z is the vertical component of the displacement vector. The last term repre-
 195 sents the advection of pre-stress, which means that the initial stress state is carried
 196 along with the particle as deformation proceeds [Wu, 2004]. The momentum equa-
 197 tion is valid for material compressibility as the buoyancy effect is neglected [Kle-
 198 mann et al., 2003, Bängtsson & Lund, 2008].

199 The difference between equation (5) and equation (6) has to be solved, when using
 200 commercial FE packages for GIA analyses. It was shown by Wu [2004], that the
 201 creation of a new stress tensor \mathbf{S}^{FE} is necessary:

$$\mathbf{S}^{FE} = \mathbf{S}^{GIA} - \rho_0 g_0 u_z \mathbf{I}, \quad (7)$$

202 where \mathbf{I} denotes the identity matrix. The product of vertical displacement and the
 203 identity matrix in the second term of equation (7) changes to the gradient of the
 204 vertical displacement by application of the divergence operator. Equation (6) can
 205 be rewritten as

$$\nabla \cdot \mathbf{S}^{FE} = 0, \quad (8)$$

206 which is identical to equation (5).

207 Stress obtained from FE models (S^{FE}) can then be modified to a GIA stress using



$$S^{GIA} = S^{FE} + \rho_0 g_0 u_z \mathbf{I}. \quad (9)$$

208 Only the diagonal components of the stress tensor are modified, whereas the shear
209 stress components from the FE model are not changed.

210 The transformation of the stress and the basic equation of motion provide several
211 boundary conditions, which are summarized in Wu [2004]. However, the displace-
212 ment is not affected by the transformation. The method has already been applied
213 in several studies, e. g. Wu [1992, 1996, 1997], Wu & Hasegawa [1996a,b], Lund
214 [2005], Wu [2009], Brandes et al. [2012], and Schmidt et al. [2012].

215 The total stress is then estimated as the combination of rebound stress determined
216 by the GIA model and background stress. The stress tensor in ABAQUS (S^{FE})
217 consists of the three diagonal elements S_{11}^{FE} , S_{22}^{FE} , and S_{33}^{FE} , while the shear stress
218 elements depend on the dimension of the model. In a 2D model, only one additional
219 stress S_{12}^{FE} is required, whereas in a 3D model all three shear stress components
220 (S_{12}^{FE} , S_{13}^{FE} , and S_{23}^{FE}) are used.

221 The stress in the model is initiated by the command `”*initial conditions,`
222 `type=stress, unbalanced stress=step”`, which is followed by the number of an
223 element and its corresponding stress values (defined below): Element-Number,
224 $S_{11}^{FE,mod}$, $S_{22}^{FE,mod}$, $S_{33}^{FE,mod}$, $S_{12}^{FE,mod}$, $S_{13}^{FE,mod}$, $S_{23}^{FE,mod}$. This line is repeated for

225 all elements, where a stress tensor is defined:

$$S_{11}^{FE,mod} = - \left(- \left(S_{11}^{FE} + (\rho_{layer} g_{layer} u_z) \right) + S_H \right), \quad (10)$$

$$S_{22}^{FE,mod} = - \left(- \left(S_{22}^{FE} + (\rho_{layer} g_{layer} u_z) \right) + S_V \right), \quad (11)$$

$$S_{33}^{FE,mod} = - \left(- \left(S_{33}^{FE} + (\rho_{layer} g_{layer} u_z) \right) + S_h \right), \quad (12)$$

$$S_{12}^{FE,mod} = - \left(- S_{12}^{FE} \right), \quad (13)$$

$$S_{13}^{FE,mod} = - \left(- S_{13}^{FE} \right), \quad (14)$$

$$S_{23}^{FE,mod} = - \left(- S_{23}^{FE} \right). \quad (15)$$

226 The first term on the right side of equations (10) to (15) is the stress due to an
 227 ice load obtained from a GIA model in ABAQUS, without any modifications. The
 228 second term on the right side of equations (10) to (12) is needed to convert the
 229 output from ABAQUS to rebound stress (after equation (9)), and depends on den-
 230 sity and gravity of the layers, and the vertical displacement from ABAQUS. The
 231 third term in equations (10) - (12) is the background stress. The third normal stress
 232 tensor component (S_{33}^{FE}) has no effect on the fault movement in a 2D model. Fur-
 233 thermore, the shear stress components S_{12}^{FE} , $S_{13}^{FE,mod}$ and $S_{23}^{FE,mod}$ are not changed
 234 by the GIA transformation and background stress components.

235 Stress values obtained and used by ABAQUS are negative for compressional con-
 236 ditions and positive for tensional regimes. In contrast, the geologic sign conven-
 237 tion typically prescribes compressional stresses with a positive sign and tensional
 238 stresses are negative. To combine both of these sign conventions, the GIA stress
 239 S^{GIA} is multiplied by -1, which results in positive stresses, and the horizontal
 240 background stress or overburden pressure are added, which are positive. The ob-
 241 tained positive total stress is used in fault stability calculations.

242 **3 Methodology**

243 Our goal is to develop a model that simulates the GIA process and releases stress
244 along faults. The implementation of an open fault contact in GIA models alters
245 the estimates of GIA stress distribution and evolution. Therefore, it is useful to
246 create a second model to capture the total stress and generate reaction forces. The
247 stresses and the reaction forces are input to a third model where the fault is opened
248 and the slip and the associated changes in stress are modelled. An inclusion of an
249 open fault contact into the GIA model directly is not possible due to the differences
250 in solving of the equation of motion between ABAQUS and GIA. Therefore, a
251 cascaded three part workflow has to be created (Fig. 2), where all models have
252 the same layers, material properties, elements, nodes, foundations, and boundary
253 conditions. The sides of all models are fixed in the horizontal direction, and no
254 velocities are applied.

255 In ABAQUS, a fault surface is defined by element faces acting upon each other,
256 whereas the element faces on opposite sides are defined by different nodes with
257 the same coordinates. One fault surface should consist of at least two elements on
258 each side of the fault. A fault is included in all three models; however, the fault is
259 not allowed to move in the first and second model. Here, the fault surface is tied
260 together, and no movement can occur. In the third model, the fault surface is open
261 and surface parameters are defined. The coefficient of friction μ is assigned a value
262 based on static friction and is the only surface parameter used in this study. The
263 cohesion cannot be defined between two fault surfaces and is thus neglected. All
264 fault commands are only allowed to be included in the model setup of an ABAQUS
265 input file. Fault commands in the step procedure cannot be used; therefore, if the
266 behaviour of the fault is changed, a new model must be created.

267 *Figure 2*

268 The methodology of including a fault into a GIA model is described in more detail
269 below and is depicted in Fig. 2:

270 [1] The first model (model 1) follows the commonly used GIA models [e. g. Wu
271 & Hasegawa, 1996a, Lund, 2005]. The earth model, consisting of a litho-
272 sphere and underlying mantle, is loaded by an ice model. In this study only
273 one glacial cycle is used. The displacement and stress tensor components are
274 computed for all times during glacial loading and unloading and results are
275 written to an output file at the end of each time point. At this point, model 1
276 itself is in quasi-static equilibrium. The fault surface is tied together so that no
277 movement can occur (definition in ABAQUS in this study: *Tie, name=fault-
278 gia, adjust=yes, type=SURFACE TO SURFACE). The complete model 1 is
279 run before the next step is used. At this point it is possible to use any kind
280 of GIA model, as only the output is used further and an open fault contact is
281 not included. Therefore, there is no feedback from a stress and displacement
282 change due to fault slip to the GIA model.

283 [2] The output of model 1 is extracted for each time point, and the full stress tensor
284 is calculated following equations (10) to (15). The new stress field is used to
285 evaluate the stability at each element. The fault stability is then calculated as
286 the mean value between all elements acting against each other along the fault
287 surface. If *CFS* along this fault is positive, a second and third model (model
288 2 and 3) are created. A negative fault stability indicates stable conditions, and
289 the output from the next time point is evaluated (see step [7]). The evolution
290 of fault stability also includes the stress changes that occurred due to any fault
291 slip.

292 [3] Model 2 consists of the same material and layer properties as model 1, and
293 the fault is still tied. This model is created for each time point obtained from
294 model 1 for which a positive CFS is obtained. No ice load is applied, and the
295 displacement from model 1 is used to define new nodal coordinates. The other
296 output parameter, the stress tensor, is changed to a total stress as calculated
297 in the analysis of the fault stability (see step [2]), which is implemented as an
298 initial condition. Consequently, the model is not in equilibrium.

299 [4] The coordinates of the nodes and the stress variables of the elements are not
300 allowed to change in model 2. However, the combination of new nodal co-
301 ordinates and new initial stress conditions leads to unstable conditions as the
302 total stress of GIA and background stress are now included. The simulation
303 of stable conditions due to the fixed movement leads to the creation of reac-
304 tion forces by ABAQUS, which are acting at each node to compensate for the
305 (additional) stress in the elements and the changed nodal coordinates. In other
306 words, ABAQUS adjusts the stress automatically, which may be appropriate
307 in engineering studies but might lead to false results for this application. As
308 not only the stress is included, but also the change in the nodal coordinates,
309 the reaction forces are not the opposite of the stress values. The reaction forces
310 applied at each node to maintain equilibrium are written to the output and are
311 used in model 3.

312 [5] In model 3 the same layer and material properties, initial stress conditions,
313 and nodal coordinates as in model 2 are used. As in model 1, the sides of
314 model 3 are not allowed to move in the horizontal direction. Furthermore, the
315 fault is opened (definition in ABAQUS in this study: *Surface Interaction,
316 name=IntProp-1; *Friction (μ); *Surface Behavior, no separation, pressure-
317 overclosure=HARD; *Contact Pair, interaction=IntProp-1, type=SURFACE

318 TO SURFACE), and the reaction forces obtained from model 2 are applied
319 (ABAQUS keyword: *Cload). The reaction forces consist of two components
320 (vertical and horizontal) in 2D applications, which have to be applied as load
321 to each node (node-number, component, value of the reaction force) in the
322 Step setup of ABAQUS. For the application of this approach in 3D models,
323 an additional reaction force component in the horizontal direction is obtained,
324 which needs to be applied in the Step setup. The movement along an open fault
325 contact is only driven by the changes in the stress field due to GIA, as the tec-
326 tonic background stress and overburden pressure are assumed to be constant
327 during the glacial period [e. g. Wu, 1996, Lund et al., 2009].

328 [6] In the case of a movement along the fault, the displacement and stresses are
329 changed. The displacement and stresses used in the input file of the fault model
330 (model 3) are referred to as d_0 and S_0 , respectively. In contrast, the output
331 obtained from model 3 with an open fault contact is called d_1 and S_1 . The
332 difference between d_1 and d_0 is the change in the displacement, and the dis-
333 placement from the output of model 1 at the following time points has to be
334 changed accordingly by this difference. The same is done for the stress tensor,
335 where the difference of S_1 to S_0 is extracted and used for all following time
336 points. Only the output for the next time points from model 1 is changed due
337 to the fault movement calculated with model 3.

338 [7] If no fault movement occurred, the differences of d_1 to d_0 and of S_1 to S_0 are
339 zero.

340 [8] The next time point is used from model 1, and the displacement ($d_1 - d_0$) and
341 stress ($S_1 - S_0$) differences from the time point before is added. The fault sta-
342 bility is evaluated again, and if the fault is found to be not stable ($CFS > 0$), a
343 new set of model 2 and 3 is created (see steps [3] - [6]). However, if the fault

344 is stable ($CFS < 0$), this set of models is not generated and the next time step
345 is analyzed.

346 The procedure described above works for any known 2D or 3D GIA model using
347 the FEM, as only the output in the form of displacement and stress is taken. Thus,
348 the GIA model itself is not affected by the fault slip, as no feedback from model 2
349 and 3 to model 1 exists.

350 **4 Model setup**

351 For this preliminary study, a flat 2D earth model is developed, which consists of six
352 layers (Fig. 3) that can be further subdivided in three different parts. The first part
353 is the mechanical lithosphere, which is composed of a 40 km thick elastic crustal
354 layer, and an elastic lithospheric mantle of 120 km. In total the lithosphere has a
355 thickness of 160 km, which is the same as in general GIA studies dealing with
356 North America [e. g. Peltier, 1984, Steffen et al., 2009]. The second part is the
357 upper mantle, which consists of two layers each with a thickness of 250 km. In
358 contrast to the lithosphere, the upper mantle is a viscoelastic layer with a viscosity
359 of $7 \cdot 10^{20}$ Pa·s [Steffen et al., 2009]. A higher viscosity of $2 \cdot 10^{22}$ Pa·s is assumed
360 for the lower mantle [Steffen et al., 2009], the third part of the earth model. This
361 viscoelastic layer is divided in two sub-layers with the same viscosity, but different
362 material parameters (Fig. 3). The rheological parameters in models 1, 2, and 3 are
363 the same.

364 Density, gravity, and Young's modulus for all layers (Fig. 3) are determined from
365 the Preliminary Reference Earth Model [PREM; Dziewonski & Anderson, 1981],
366 and the viscosity values are obtained from general GIA studies constrained by ob-
367 served data in North America. The sides of the earth model are fixed in the hori-

368 zontal direction.

369 To account for the restoring buoyancy force that drives GIA, so-called Winkler
370 foundations are used in the model (ABAQUS keyword: *Foundation), which are
371 applied along boundaries with density contrasts. The Winkler foundations are cal-
372 culated from the density contrast along the boundary and the gravity in the lower
373 layer [Wu, 2004].

374 The earth model of this study includes a fault surface without density contrast.
375 Details about the location and parameters of the fault can be found in the next sec-
376 tion. Quadrilateral plane strain elements with 4 nodes (ABAQUS keyword: CPE4)
377 are used for all layers. In the crustal layer, the elements have a side length of ap-
378 proximately 700 m. The size of the elements increases in the following layers and
379 reaches ca. 200 km in the lowest layer. The mesh consist of 327,666 elements.

380 *Figure 3*

381 On the top of the earth model, a parabolic ice model (Fig. 3) is applied during
382 glaciation (ABAQUS keyword: *Dload), which simulates the last glacial period
383 in North America. The ice sheet has a maximum thickness of 3500 m at glacial
384 maximum, and a width of 3000 km. It was shown by Amelung & Wolf [1994]
385 that flat models without self-gravity can be used for the estimation of deformations
386 inside the ice margin for large ice sheets (e. g. an ice-sheet width of 3000 km). To
387 account for the size of the ice sheet and to avoid boundary effects, the model has a
388 width of 40,000 km and a depth of 2891 km (approximately core-mantle boundary).
389 The initial time is before glaciation, thus no ice is applied on the Earth's surface.
390 The volume of the ice sheet increases linearly for 100 ka, and decreases in the
391 following 10 ka. For simplicity, the horizontal dimension of the ice sheet is not
392 changed during the glacial period, i. e. there is no migration of the ice margin.

393 The new GIA model with a fault, which is a combination of earth and applied
394 ice model, runs from the beginning of loading to 30 ka after glacial maximum.
395 131 time points are created during the run of the model with a time step of 1 ka.
396 The combination of all three models runs in ~ 36 hours on a UNIX 2.27 GHz dual-
397 core processor and 3.5 GB of RAM.

398 **5 The response of a fault due to GIA**

399 The example model includes a fault from the surface to a depth of 8 km located at
400 the centre of the ice sheet. The fault dips at 45° , giving a value for Θ of 45° for the
401 first time point following equation (2). For the first time point, the maximum prin-
402 cipal stress is horizontal, and Θ is the angle between the normal of the fault to the
403 horizontal direction. Due to the changing stress directions and fault movements,
404 the shear stress increases and the third term in equation (2) is not zero anymore.
405 Therefore, a change in the angle Θ cannot be neglected; however, the fault angle α
406 stays constant. The fault surface in this model consists of 10 elements on each side
407 of the fault.

408 The tectonic background stress in northeastern Canada is characterized by a thrust-
409 ing regime [e. g. Zoback, 1992, Mazzotti & Townend, 2010, Steffen et al., 2012].
410 A fault angle of 45° is chosen as it represents the mean value between the opti-
411 mally orientated fault angle of 30° for the thrusting regime and the observed angle
412 of GIFs of about 60° [Fenton, 1994, Juhlin et al., 2009, Brandes et al., 2012].

413 The fault is described by a friction coefficient of 0.6 and negligible cohesion along
414 the fault (ABAQUS does not allow the inclusion of a cohesion value as a contact
415 property). For simplicity, zero pore pressure is assumed, which leads to a pore-fluid
416 factor λ_f of 0.

417 Table 1 gives values for the horizontal background stress and overburden pressure at
418 three depths (1 km, 10 km, and 15 km) obtained using equations (4) and (3), respec-
419 tively. The horizontal background stress is the summation of overburden pressure
420 and tectonic background stress, and depends not only on the depth, but also on the
421 angle of the fault (45°) and coefficient of friction (0.6) to keep the fault at frictional
422 equilibrium before the onset of glaciation. Similar stress values at lower depth are
423 obtained for a dry granitic crust [Shimada, 1993].

424 *Table 1*

425 The response of the GIA model shows the greatest vertical displacement below the
426 maximum load at glacial maximum (-594 m). At 1900 km distance from the centre
427 of the model, the peripheral bulge shows the maximum values for the positive verti-
428 cal displacement (59 m). At glacial maximum, the axis of tilting, which is indicated
429 by the changeover of the vertical displacement from negative to positive values,
430 occurs at 1600 km, just outside of the ice sheet.

431 Fig. 4 shows the horizontal rebound stress behaviour at glacial maximum (a), at the
432 end of deglaciation (c), and 10 ka after the end of deglaciation (e), when no fault
433 is included. The vertical and horizontal background stresses are both larger than
434 the GIA stress (Table 1, Fig. 4), and are therefore removed for the visualization.
435 The highest values of horizontal rebound stresses are obtained at glacial maximum
436 (Fig. 4(a)), but the values decrease only slowly with 21 MPa at glacial maximum
437 to 14 MPa 10 ka after the end of deglaciation at the surface (Fig. 4(c,e)). In con-
438 trast, the vertical loading stress is decreased from ~ 30 MPa at glacial maximum to
439 0 MPa at the end of deglaciation and remains zero afterwards.

440 The total stress determined by the background stress (see Table 1) and the rebound
441 stress vary between a few MPa and several thousands of MPa with increasing depth.

442 To account for the stresses in the elements in model 2, reaction forces between -
443 $9.6 \cdot 10^{23}$ N and $9.6 \cdot 10^{23}$ N had to be applied at 2 ka before the end of deglaciation.
444 The highest values were obtained close to the sides of the model at depths of about
445 2700 km, as in this part the stresses are changing from several MPa to 0 MPa out-
446 side the model.

447 *Figure 4*

448 The fault below the ice-sheet centre is stable for most of the time and becomes
449 unstable 2 ka before the end of deglaciation. The fault stability at this location,
450 which is determined in a subroutine, allows the opening of the fault contact and
451 movement can occur. The fault slips during the earthquake with a maximum of
452 22 m at 2 km depth. Fault slip decreases towards the fault tip and surface, giving a
453 surface fault scarp of 19.74 m (Fig. 5). It was shown by Kim & Sanderson [2005]
454 that the fault slip decreases towards the tips and is the maximum in the middle
455 between both tips. However, only one fault tip is used here and the other side is
456 open at the surface. One might expect the largest fault slip to be along the surface,
457 but the combination of background stress, which increases with depth, and rebound
458 stress, which decreases with depth, creates larger stresses at 2 km below the surface.
459 Nevertheless, the total stress increases with depth, but the fixed fault tip prevents
460 further movement, and the slip decreases between 2 km and the fault tip, which lies
461 at 8 km depth.

462 The fault movement releases most of the GIA stress along the fault, and stress is
463 accumulated only at the lower part of the fault as the fault tip is fixed and cannot
464 slip (Fig. 4(d)). These large stresses were found in other studies as well, if a fixed
465 fault tip is used [e. g. Schlagenhauf et al., 2008]. The stress might be released in
466 post-seismic creep, which is not considered in this model. No other parts along

467 the fault, excluding the fault tip, are critically stressed again (Fig. 4 (f)). Therefore,
468 no movement occurs at subsequent time points. However, faults at other locations
469 might be activated due to the GIA stress.

470 The time of fault slip is also visible in the distribution of fault stability (*CFS*) and
471 normal and shear stress evolution along the fault plane (Fig. 6). At the surface and at
472 4 km depth, shear and normal stress decrease by several MPa after the fault slipped.
473 The change in normal and shear stress depends on the magnitude of these stresses
474 before the fault was activated. The increase in *CFS* before fault activation is similar
475 at all depths, but changes by about 100 MPa at the fault tip and only 7 MPa at the
476 surface. The normal stress at 8 km depth increases after fault movement, which is
477 not found for other depths and the shear stress. This might be related to the large
478 stress build-up at the tip. After the fault slipped, no change in shear and normal
479 stresses and fault stability is obtained.

480 *Figure 5*

481 *Figure 6*

482 The distribution of the vertical displacement shows an upward motion of the hang-
483 ing wall and a downward motion of the footwall (Fig. 7), indicative of a thrust-
484 ing/reverse earthquake. The vertical displacement ranges between 12.5 m and -
485 3.1 m, whereas in the far field of the fault the vertical displacement is 0 m. This
486 is in agreement with the analytical solution obtained after Okada [1985] using an
487 elastic half-space, which varies between 12.3 m and -3.0 m (Fig. 7, dashed red line).
488 The analytical solution is obtained using the programme by Beauducel [2012]
489 based on the values of the geometry of the rectangular fault (length, width, depth,
490 strike, dip), the sense of movement (rake value, which is 90° for a thrust/reverse
491 fault), and the fault slip. The behaviour of the fault movement is similar for mod-


492 elled and analytical solution, which verifies our implementation of fault reactivation
493 and slip in the GIA model.

494 *Figure 7*

495 **6 Conclusions**

496 In this paper we introduce a new approach to implement slip on a fault in general
497 GIA models, which can be applied to large and small ice sheets. Our technique is
498 applicable to any GIA model using the finite-element method. A cascaded three-
499 step approach is used, in which the first is based on commonly used GIA models.
500 An ice model is applied on top of an earth model, which includes a tied fault contact
501 in the upper crust. The second step uses the results of the first model for each time
502 point. The displacement is applied to change the nodal coordinates, and the stress
503 is changed according to the theory of Wu [2004] by adding horizontal and vertical
504 background stresses. The stress provides the initial conditions for the elements. The
505 stress values together with the nodal coordinates are not in equilibrium, and both
506 values are not allowed to change. In order to maintain equilibrium, reaction forces
507 are applied. These forces oppose the applied stress and are estimated by fixing all
508 degrees of freedom. In the third step, the fault contact is opened to release the GIA
509 stress. The fault is only driven by the stress changes due to GIA, as horizontal and
510 vertical stresses are assumed to be constant and no velocities are applied at the sides
511 of the model.

512 Our approach is illustrated using an example with a 45°-dipping fault. Slip of up
513 to 22 m is modelled to occur at the end of deglaciation, creating a fault scarp of
514 19.74 m. The fault slip decreases with depth below 2 km. The vertical displacement
515 shows that the earthquake is characterized by a thrusting/reverse mechanism, con-

516 sistent with field observations [e. g. Lagerbäck, 1978]. The GIA stress is released
517 with this earthquake, but at the fault tip stress is still concentrated, which may be
518 released in post-seismic creep, but this is not part of the current model. 
519 ~~In the future,~~ changes in the fault parameters (length, μ , C) as well as different
520 locations, dipping angles, and ~~the~~ pore-fluid pressure will be tested. Additionally,
521 ~~the~~ background stress conditions ~~can be changed to a~~ normal regime or strike-slip
522 regime. Further possible parameters, ~~which~~ can be tested, ~~are~~ the magnitude of tec-
523 tonic background stress, and changes in earth and ice model.

524 In general, the development of this model algorithm enables the inclusion of more
525 realistic faults within GIA models. This combination is expected to yield a better
526 understanding of glacially induced faults, and what can be expected for regions
527 where deglaciation is ongoing (e. g. Greenland).

528 **Acknowledgments**

529 We are very grateful for the excellent reviews and numerous valuable suggestions
530 from two anonymous referees and the editor Jef Caers, which have greatly im-
531 proved this manuscript. Special thanks goes to Björn Lund and Peter Schmidt (both
532 from Uppsala University), and Steffen Abe (RWTH Aachen), for helpful discus-
533 sions, and to Len Hills (University of Calgary) for suggestions and comments on
534 earlier versions of the manuscript. The research was supported by NSERC Discov-
535 ery Grants to David W. Eaton and Patrick Wu, and a Research Grant to Rebekka
536 Steffen by the International Association of Mathematical Geosciences. Figures 4, 5,
537 and 7 in this paper are drawn or prepared using the GMT graphics package [Wessel
538 & Smith, 1998].

539 **References**

- 540 Abers, G.A. (2009): Slip on shallow-dipping normal faults, *Geology*, **37**, 767-768,
541 doi:10.1130/focus082009.1.
- 542 Adams, J. (1989a): Postglacial faulting in eastern Canada: nature, origin and
543 seismic hazard implications, *Tectonophysics*, **163**, 323-331, doi:10.1016/0040-
544 1951(89)90267-9.
- 545 Adams, J. (1989b): Crustal stresses in eastern Canada, *In: Gregersen, S. & Basham,*
546 *P.W. (eds), Earthquakes at North Atlantic Passive Margins: Neotectonics and*
547 *Postglacial Rebound*, Kluwer, Dordrecht, 289-297.
- 548 Adams, J., Wetmiller, R.J., Hasegawa, H.S., Drysdale, J. (1991): The first surface
549 faulting from a historical intraplate earthquake in North America, *Nature*, **352**,
550 617-619, doi:10.1038/352617a0.
- 551 Amelung, F., Wolf, D. (1994): Viscoelastic perturbations of the earth: significance
552 of the incremental gravitational force in models of glacial isostasy, *Geophys. J.*
553 *Int.*, **117**, 864-879, doi:10.1111/j.1365-246X.1994.tb02476.x.
- 554 Anderson, E.M. (1951): The dynamics of faulting and dyke formation with appli-
555 cations to Britain, *Oliver & Boyd*, Edinburgh, UK, 2nd Edition.
- 556 Arvidsson, R. (1996): Fennoscandian Earthquakes: Whole Crustal
557 Rupturing Related to Postglacial Rebound, *Science*, **274**, 744-746,
558 doi:10.1126/science.274.5288.744.
- 559 Bängtsson, B., Lund, B. (2008): A comparison between two solution techniques to
560 solve the equations of glacially induced deformation of an elastic Earth, *Int. J.*
561 *Numer. Meth. Engng*, **75**, 479-502, doi:10.1002/nme.2268.
- 562 Beauducel, F. (2012): Okada: Surface deformation due to a fi-
563 nite rectangular source, Published Matlab programme at
564 <http://www.mathworks.com/matlabcentral/fileexchange/25982>.

- 565 Bonini, M., Sani, F., Antonielli, B. (2012): Basin inversion and contrac-
566 tional reactivation of inherited normal faults: A review based on pre-
567 vious and new experimental models, *Tectonophysics*, **522-523**, 55-88,
568 doi:10.1016/j.tecto.2011.11.014.
- 569 Brandes, C., Winsemann, J., Roskosch, J., Meinsen, J., Tanner, D.C., Tsukamoto,
570 S., Frechen, M., Steffen, H., Wu, P. (2012): Activity along the Osning Thrust
571 in Central Europe during the late Weichselian: ice-sheet and lithosphere interac-
572 tions, *Quat. Sci. Rev.*, **38**, 49-62, doi:10.1016/j.quascirev.2012.01.021.
- 573 Cathles, L.M. (1975): The Viscosity of the Earth's Mantle, *Princeton University*
574 *Press*, Princeton, USA.
- 575 Dyke, A.S., Morris, T.F., Green, D.E.C. (1991): Postglacial tectonic and sea level
576 history of the central Canadian Arctic, *Geological Survey of Canada Bulletin*,
577 **397**.
- 578 Dziewonski, A.M., Anderson, D.L. (1981): Preliminary reference Earth model,
579 *Phys. Earth planet. Inter.*, **25**, 297-356, doi:10.1016/0031-9201(81)90046-7.
- 580 Fenton, C. (1994): Postglacial faulting in Eastern Canada, *Geological Survey of*
581 *Canada - Open File*, **2774**.
- 582 Hampel, A., Hetzel, R. (2006): Response of normal faults to glacial-interglacial
583 fluctuations of ice and water masses on Earths surface, *J. Geophys. Res.*, **111**,
584 B06406, doi:10.1029/2005JB004124.
- 585 Hampel, A., Hetzel, R., Maniatis, G., Karow, T. (2009): Three-dimensional
586 numerical modeling of slip rate variations on normal and thrust fault ar-
587 rays during ice cap growth and melting, *J. Geophys. Res.*, **114**, B08406,
588 doi:10.1029/2008JB006113.
- 589 Harris, R.A. (1998): Introduction to special section: Stress triggers, stress shad-
590 ows, and implications for seismic hazard, *J. Geophys. Res.*, **103**, 24347-24358,

591 doi:10.1029/98JB01576.

592 Heibach, O., Tingay, M., Barth, A., Reinecker, J., Kurfe, D., Miller, B. (2008): The
593 World Stress Map database release 2008, doi:10.1594/GFZ.WSM.Rel2008.

594 Hetzel, R., Hampel, A. (2005): Slip rate variations on normal faults dur-
595 ing glacial-interglacial changes in surface loads, *Nature*, **435**, 81-84,
596 doi:10.1038/nature03562.

597 Hibbitt, D., Karlsson, B., Sorensen, P. (2011): Getting Started with ABAQUS -
598 Version (6.11), Hibbitt, Karlsson & Sorensen, Inc.

599 Johnston, A.C. (1987): Suppression of earthquakes by large continental ice sheets,
600 *Nature*, **330**, 467-469, doi:10.1038/330467a0.

601 Johnston, P., Wu, P., Lambeck, K. (1998): Dependence of horizontal stress magni-
602 tude on load dimension in glacial rebound models, *Geophys. J. Int.*, **132**, 41-60,
603 doi:10.1046/j.1365-246x.1998.00387.x.

604 Juhlin, C., Dehghannejad, M., Lund, B., Malehmir, A., Pratt, G. (2009): Reflec-
605 tion seismic imaging of the end-glacial Pärvie Fault system, northern Sweden, *J.*
606 *Appl. Geophys.*, **70**, 307-316, doi:10.1016/j.jappgeo.2009.06.004.

607 Kim, Y.-S., Sanderson, D.J. (2005): The relationship between displace-
608 ment and length of faults: a review, *Ear. Sci. Rev.*, **68**, 317-334,
609 doi:10.1016/j.earscirev.2004.06.003.

610 Klemann, V., Wolf, D. (1998): Modelling of stresses in the Fennoscandian
611 lithosphere induced by Pleistocene glaciations, *Tectonophysics*, **294**, 291-303,
612 doi:10.1016/S0040-1951(98)00107-3.

613 Klemann, V., Wu, P., Wolf, D. (2003): Compressible viscoelasticity: stability of
614 solutions for homogeneous plane-Earth models, *Geophys. J. Int.*, **153**, 569-585,
615 doi:10.1046/j.1365-246X.2003.01920.x.

616 Kujansuu, R. (1964): Nuorista siirroksista Lappissa. Summary: Recent faults in

- 617 Lapland, *Geologi*, **16**, 30-36.
- 618 Lagerbäck, R. (1978): Neotectonic structures in northern Sweden, *Ge-*
619 *ologiska Föreningen i Stockholm Förhandlingar*, **100**, 263-269,
620 doi:10.1080/11035897809452533.
- 621 Lanaro, F., Öhman, J., Fredriksson, A. (2006). Rock mechanics modelling of rock
622 mass properties - summary of primary data, *Swedish Nuclear Fuel and Waste*
623 *Management Co.*, Stockholm, Report R-06-15, 68 pp..
- 624 Lund, B. (2005): Effects of deglaciation on the crustal stress field and implica-
625 tions for endglacial faulting: A parametric study of simple Earth and ice models,
626 *Swedish Nuclear Fuel and Waste Management Co.*, Stockholm, Technical Report
627 TR-05-04, 68 pp..
- 628 Lund, B., Zoback, M.D. (1999): Orientation and magnitude of in situ stress to
629 6.5 km depth in the Baltic Shield, *Int. J. Rock. Mech. Min. Sci.*, **36**, 169-190,
630 doi:10.1016/S0148-9062(98)00183-1.
- 631 Lund, B., Schmidt, P., Hieronymus, C. (2009): Stress evolution and fault stability
632 during the Weichselian glacial cycle, *Swedish Nuclear Fuel and Waste Manage-*
633 *ment Co.*, Stockholm, Technical Report TR-09-15, 101 pp..
- 634 Mazotti, S., Townend, J. (2010): State of stress in central and eastern North Amer-
635 ican seismic zones, *Lithosphere*, **2**, 76-83, doi:10.1130/L65.1.
- 636 Ni, Z., Wu, P. (1998): Effects of removing concentric positioning on postglacial
637 vertical displacement in the presence of lateral variation in lithospheric thickness,
638 *Geophys. Res. Lett.*, **25**, 3209-3212, doi:10.1029/98GL52326 .
- 639 Okada, Y. (1985): Surface deformation due to shear and tensile faults in a half-
640 space, *Bull. Seismol. Soc. Am.*, **75**, 1135-1154.
- 641 Olesen, O. (1988): The Stuuragurra Fault, evidence of neotectonics in the Precam-
642 brian of Finnmark, northern Norway, *Norsk Geologisk Tidsskrift*, **68**, 107-118.

- 643 Peltier, W.R. (1984): The Thickness of the Continental Lithosphere, *J. Geophys.*
644 *Res.*, **89**, B13, 11303, doi:10.1029/JB089iB13p11303.
- 645 Peltier, W.R. (2004): Global Glacial Isostasy and the Surface of the Ice-Age Earth:
646 The ICE-5G (VM2) Model and GRACE, *Annu. Rev. Earth Planet. Sci.*, **32**, 111-
647 149, doi:10.1146/annurev.earth.32.082503.144359.
- 648 Quinlan, G. (1984): Postglacial rebound and the focal mechanisms of eastern Cana-
649 dian earthquakes, *Can. J. Earth Sci.*, **21**, 1018-1023, doi:10.1139/e84-106.
- 650 Ranalli, G. (1995): Rheology of the Earth, *Chapman & Hall*, London, UK, 2nd
651 edition.
- 652 Shimada, M. (1993): Lithospheric strength inferred from fracture strength of
653 rocks at high confining pressures and temperatures, *Tectonophysics*, **217**, 55-64,
654 doi:10.1016/0040-1951(93)90202-U.
- 655 Schlagenhauf, A., Manighetti, I., Malavieille, J., Dominguez, S. (2008): Incremen-
656 tal growth of normal faults: Insights from a laser-equipped analog experiment,
657 *Earth planet. Sci. Lett.*, **273**, 299-311, doi:10.1016/j.epsl.2008.06.042.
- 658 Schmidt, P., Lund, B., Hieronymus, C. (2012): Implementation of the glacial re-
659 bound prestress advection correction in general-purpose finite element analysis
660 software: Springs versus foundations, *Computers & Geosciences*, **40**, 97-106,
661 doi:10.1016/j.cageo.2011.07.017.
- 662 Slunga, R. (1991): The Baltic shield earthquakes, *Tectonophysics*, **189**, 323-331,
663 doi:10.1016/0040-1951(91)90505-M.
- 664 Spada, G., Barletta, V.R., Klemann, V., Riva, R.E.M., Martinec, Z., Gasperini,
665 P., Lund, B., Wolf, D., Vermeersen, L.L.A., King, M.A. (2011): A benchmark
666 study for glacial isostatic adjustment codes, *Geophys. J. Int.*, **185**, 106-132,
667 doi:10.1111/j.1365-246X.2011.04952.x.
- 668 Steffen, H., Wu, P. (2011): Glacial isostatic adjustment in Fennoscan-

669 dia - A review of data and modeling, *J. Geodyn.*, **52**(3-4), 169-204,
670 doi:10.1016/j.jog.2011.03.002.

671 Steffen, H., Müller, J., Denker, H. (2009): Analysis of Mass Variations in Northern
672 Glacial Rebound Areas from GRACE Data, Springer, IAG Symposia Series, ed.
673 M. Sideris, 501-509, doi:10.1007/978-3-540-85426-5_60.

674 Steffen, R., Eaton, D.W., Wu, P. (2012): Moment tensors, state of stress and their
675 relation to post-glacial rebound in northeastern Canada, *Geophys. J. Int.*, **189**,
676 1741-1752, doi:10.1111/j.1365-246X.2012.05452.x.

677 Turcotte, D.L., Schubert, G. (2002): Geodynamics, *Cambridge University Press*,
678 Cambridge, UK, 2nd edition.

679 Twiss, R.J., Moores, E.M. (2007): Structural Geology, *W.H. Freeman and Com-*
680 *pany*, New York, USA, 2nd edition.

681 van der Wal, W., Wu, P., Wang, H., Sideris, M. (2010): Sea levels and uplift rate
682 from composite rheology in glacial isostatic adjustment modeling, *J. Geodyn.*,
683 **50**, 38-48, doi:10.1016/j.jog.2010.01.006.

684 Wang, H., Wu, P. (2006): Effects of lateral variations in lithospheric thickness and
685 mantle viscosity on glacially induced relative sea levels and long wavelength
686 gravity field in a spherical, self-gravitating Maxwell Earth, *Earth planet. Sci.*
687 *Lett.*, **249**, 368-383, doi:10.1016/j.epsl.2006.07.011.

688 Wessel, P., Smith, W.H.F. (1998): New, improved version of generic mapping tools
689 released, *EOS, Trans. Am. geophys. Un.*, **79**, 579.

690 Wu, P. (1992): Viscoelastic versus viscous deformation and the advection of pre-
691 stress, *Geophys. J. Int.*, **108**, 136-142, doi:10.1111/j.1365-246X.1992.tb00844.x.

692 Wu, P. (1996): Changes in orientation of near-surface stress field as constraints to
693 mantle viscosity and horizontal stress differences in Eastern Canada, *Geophys.*
694 *Res. Letters*, **23**, 2263-2266, doi:10.1029/96GL02149.

- 695 Wu, P. (1997): Effect of viscosity structure on fault potential and stress orien-
696 tations in eastern Canada, *Geophys. J. Int.*, **130**, 365-382, doi:10.1111/j.1365-
697 246X.1997.tb05653.x.
- 698 Wu, P. (1999): Modeling Postglacial Sea-Levels with Power Law Rheology and
699 Realistic Ice Model in the Absence of Ambient Tectonic Stress, *Geophys. J. Int.*,
700 **139**, 691-702, doi:10.1046/j.1365-246x.1999.00965.x.
- 701 Wu, P. (2004): Using commercial Finite element packages for the study of earth
702 deformations, sea levels and the state of stress, *Geophys. J. Int.*, **158**, 401-408,
703 doi:10.1111/j.1365-246X.2004.02338.x.
- 704 Wu, P. (2009): State-of-the-Science Review of the Stress Field during a Glacial
705 Cycle and Glacial Induced Faulting, *Nuclear Waste Management Organization*,
706 Technical Report TR-2009-09, 84 pp..
- 707 Wu, P., Hasegawa, H.S. (1996a): Induced stresses and fault potential in Eastern
708 Canada due to a disc load: a preliminary analysis, *Geophys. J. Int.*, **125**, 415-
709 430, doi:10.1111/j.1365-246X.1996.tb00008.x.
- 710 Wu, P., Hasegawa, H.S. (1996b): Induced stresses and fault potential in eastern
711 Canada due to a realistic load: a preliminary analysis, *Geophys. J. Int.*, **127**, 215-
712 229, doi:10.1111/j.1365-246X.1996.tb01546.x.
- 713 Wu, P., Steffen, H., Wang, H. (2010): Optimal locations for GPS measurements in
714 North America and northern Europe for constraining Glacial Isostatic Adjust-
715 ment, *Geophys. J. Int.*, **181**, 653-664, doi:10.1111/j.1365-246X.2010.04545.x.
- 716 Wu, P., Wang, H., Steffen, H. (2013): The Role of Thermal Effect on Mantle Seis-
717 mic Anomalies under Laurentia and Fennoscandia from Observations of Glacial
718 Isostatic Adjustment, *Geophys. J. Int.*, **192**, 7-17, doi:10.1093/gji/ggs009.
- 719 Zoback, M.L. (1992): Stress Field Constraints on Intraplate Seismicity in Eastern
720 North America, *J. Geophys. Res.*, **97**, 11761-11782, doi:10.1029/92JB00221.

721 Zoback, M.D., Townend, J. (2001): Implications of hydrostatic pore pressures
722 and high crustal strength for the deformation of intraplate lithosphere, *Tectono-*
723 *physics*, **336**, 19-30, doi:10.1016/S0040-1951(01)00091-9.

724 Captions to Figures:

725

726 **Figure 1:**

727 Definition of the Mohr circle using the maximum and minimum principal stress
728 magnitudes σ_1 and σ_3 , and the definition of the fault stability value *CFS* depending
729 on the fault angle α (inset). The line of failure is given for a fault without cohesion
730 and with cohesion (red). The coefficient of friction μ , the normal stress σ_n and the
731 shear stress τ are used for both equations. The angle Θ is related to the dipping
732 angle of the fault α by equation (2).

733

734 **Figure 2:**

735 Flowchart illustrating the steps of the methodology.

736

737 **Figure 3:**

738 Structure of the model used for the implementation of faults. Springs represent
739 foundations used in the model, triangles represent the fixed degree of freedom
740 along the sides of the model, and the red line shows the fault in the crustal layer.
741 The ice sheet follows a parabolic shape without any change in the horizontal
742 dimension (grey body on top of the model). Density ρ , Young's modulus E ,
743 Poisson's ratio ν , viscosity η , gravity g and thickness values are given for each
744 layer [after Dziewonski & Anderson, 1981, Steffen et al., 2009]. This model setup
745 is used in all three models.

746

747 **Figure 4:**

748 Horizontal stress component of the GIA stress for a model without fault (left) and
749 with fault (right) for three different time points: (a, b) glacial maximum, (c, d) 2 ka
750 before the end of deglaciation (at time of fault movement), (e, f) 10 ka after end
751 of deglaciation. Tectonic background stress and overburden pressure are removed.
752 The black line indicates the fault, and the purple line on top shows the location of
753 the ice sheet during the glacial period. Noise level is due to finite-element structure
754 and interpolation for plotting purposes.

755

756 **Figure 5:**

757 Fault slip along the fault at five depths during the last 30 ka of the GIA model. The
758 purple line shows the load applied to the model.

759

760 **Figure 6:**

761 Normal stress, shear stress and fault stability (*CFS*) along the fault surface between
762 100 ka (maximum glaciation) and 130 ka. The values are calculated at three depths
763 along the fault surface: 0.5 km (surface, blue), 4 km (mid of the fault, green), and
764 8 km (fault tip, red). The purple line shows the load applied to the model.

765

766 **Figure 7:**

767 Vertical displacement variation at 108 ka along the surface in 1D obtained from
768 this model (black solid line) and calculated after Okada [1985] using an elastic
769 half-space (dashed red line). The purple line indicates the location of the ice sheet
770 during the glacial period.

771

Table 1

Stress magnitudes for overburden pressure and horizontal background stress at several depths. Note that the horizontal background stress in the model is the summation of tectonic background stress and overburden pressure.

Depth	Horizontal background stress	Overburden pressure
1 km	128 MPa	32 MPa
10 km	1282 MPa	320 MPa
15 km	1923 MPa	481 MPa

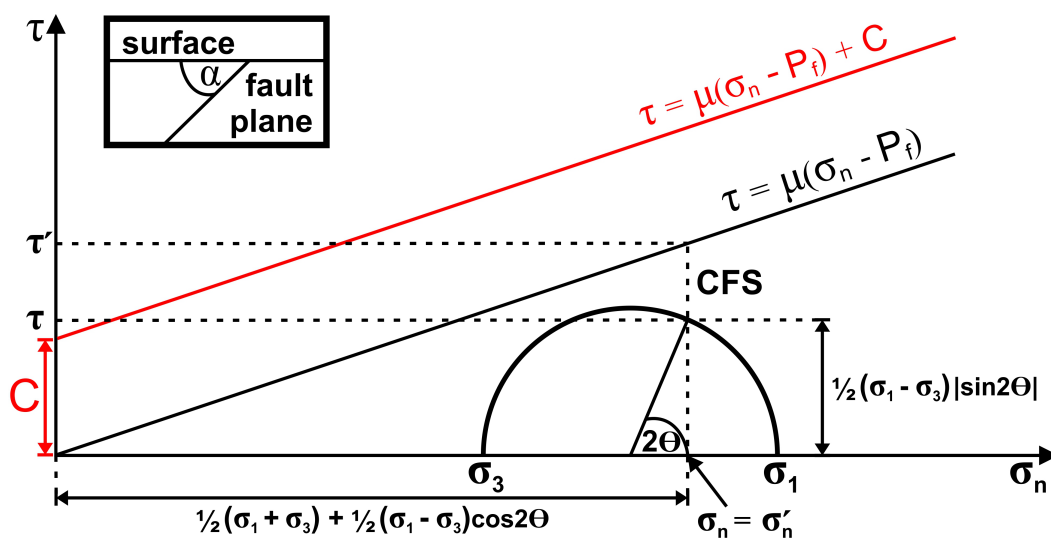


Fig. 1.

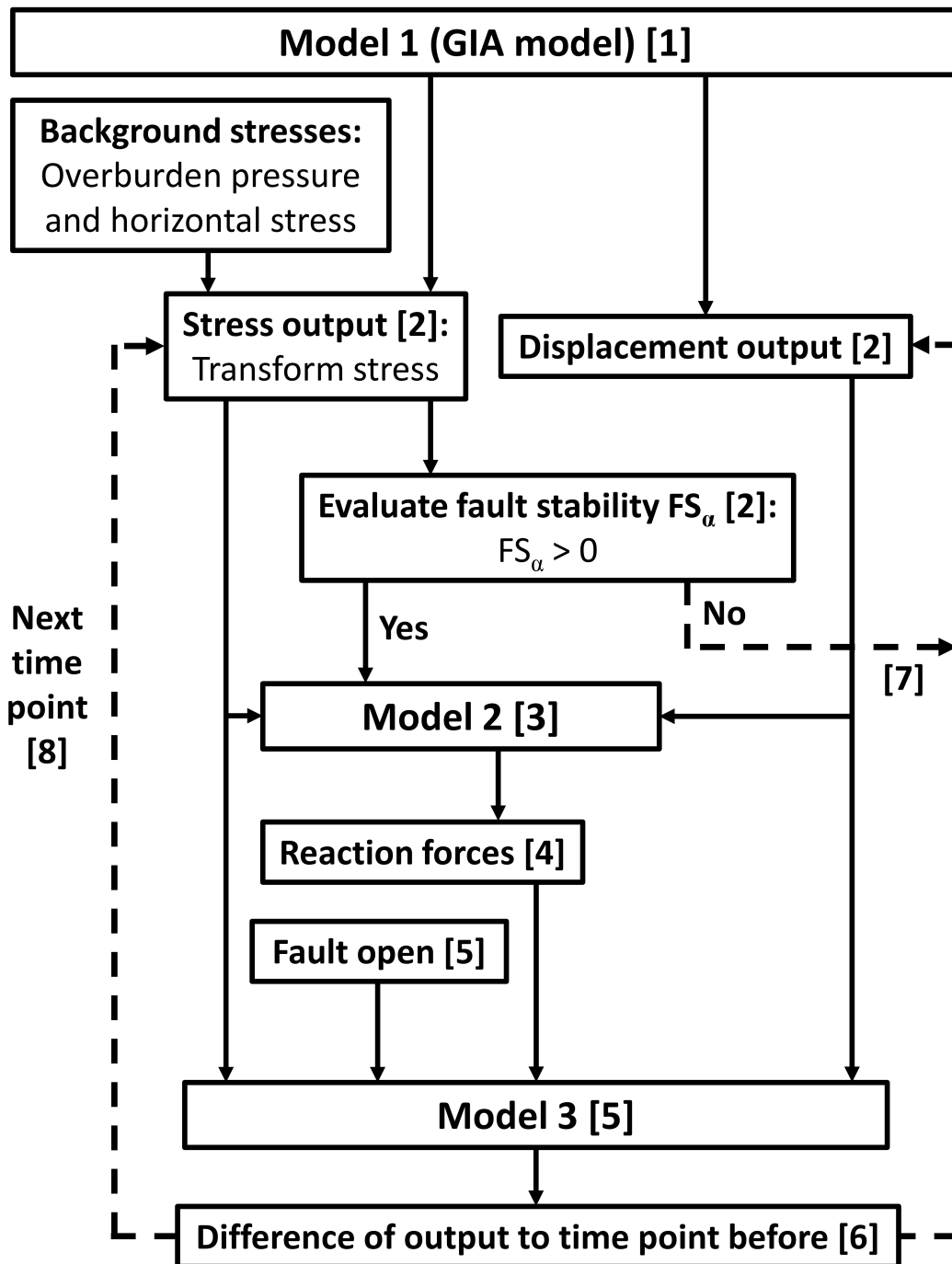


Fig. 2.

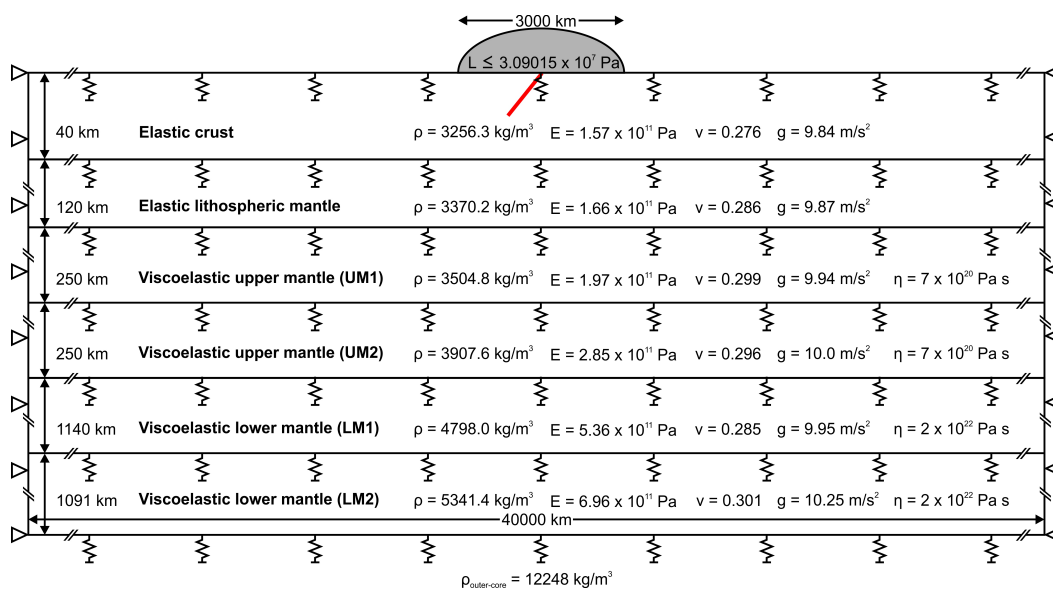


Fig. 3.

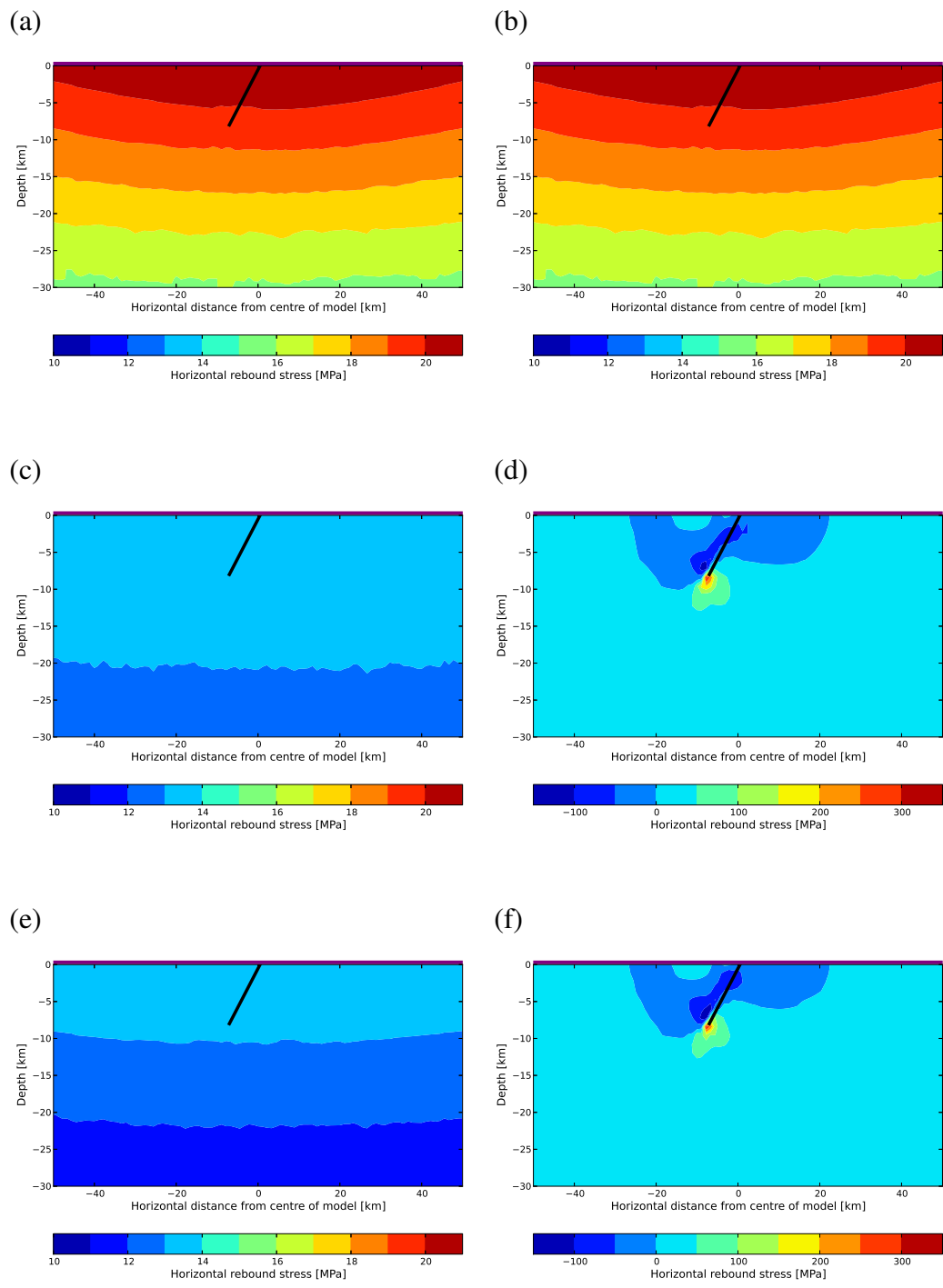


Fig. 4.

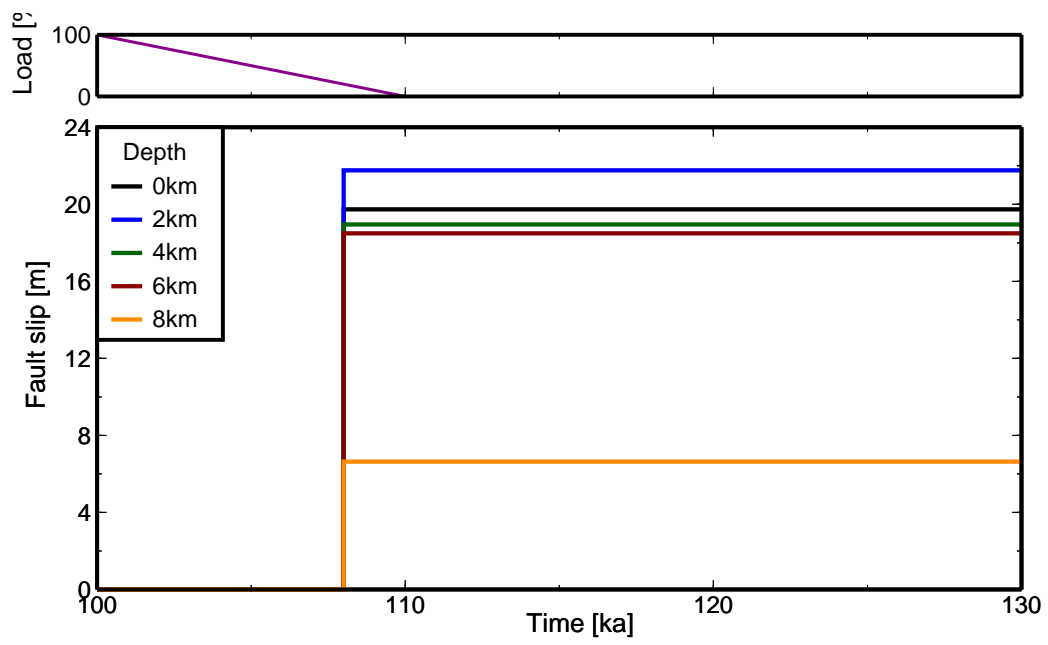


Fig. 5.

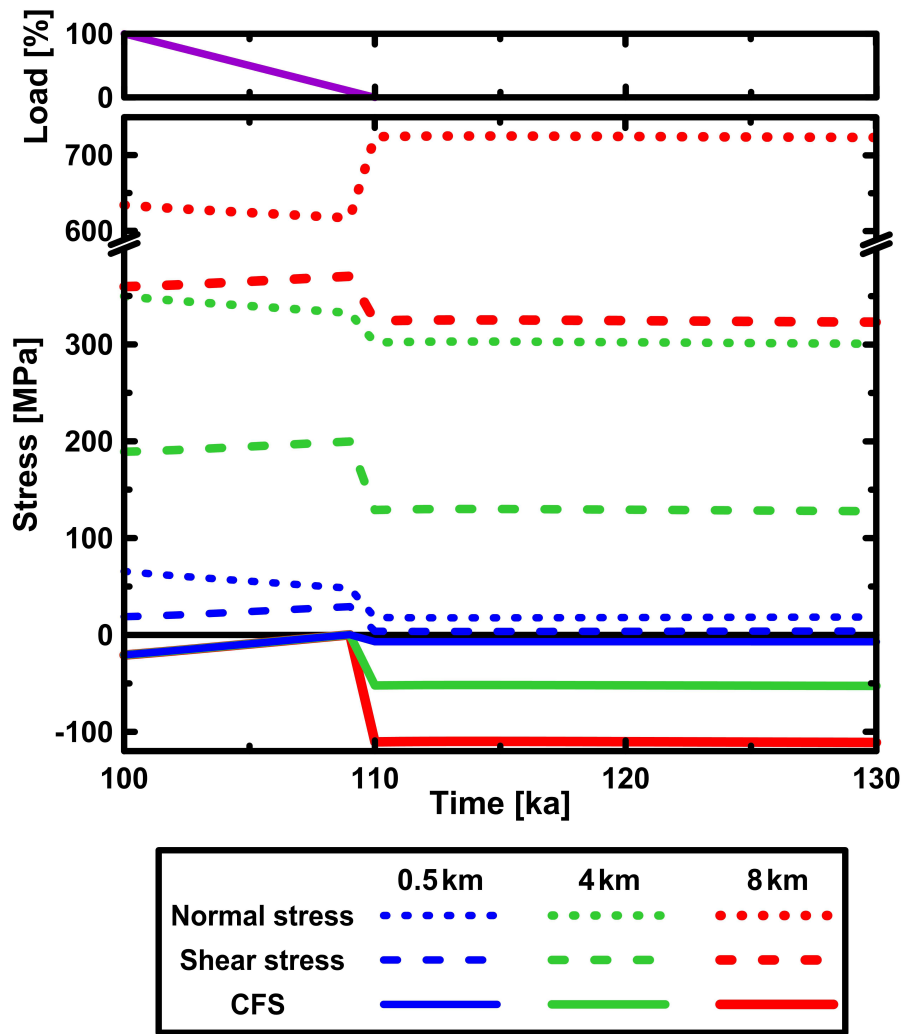


Fig. 6.

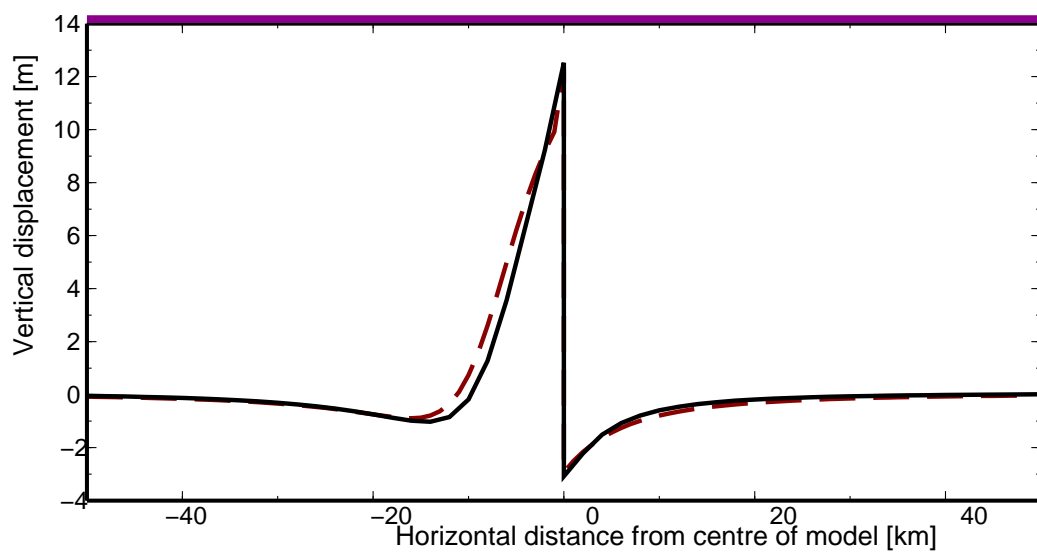


Fig. 7.